Citation: Sun, Z., Schrijer, F. F. J., Scarano, F. & van Oudheusden, B. W. (2014). Decay of the supersonic turbulent wakes from micro-ramps. Physics of Fluids, 26(2), 025115. doi: 10.1063/1.4866012

Decay of the Supersonic Turbulent Wakes from Micro-ramps

Z. Sun,[1] F. F. J. Schrijer, F. Scarano, and B. W. van Oudheusden
Faculty of Aerospace Engineering, Delft University of Technology,
Kluyverweg 2, 2629HS Delft, the Netherlands

The wakes resulting from micro-ramps immersed in a supersonic turbulent boundary layer at *Ma*=2.0 are investigated by means of particle image velocimetry (PIV). Two micro-ramps are investigated with height of 60% and 80% of the undisturbed boundary layer, respectively. The measurement domain is placed at the symmetry plane of the ramp and encompasses the range from 10 to 32 ramp heights downstream of the ramp. The decay of the flow field properties is evaluated in terms of time-averaged and root-mean-square (RMS) statistics. In the time-averaged flow field, the recovery from the imparted momentum deficit and the decay of upwash motion are analyzed. The RMS fluctuations of the velocity components exhibit strong anisotropy at the most upstream location and develop into a more isotropic regime downstream. The self-similarity properties of velocity components and fluctuation components along wall-normal direction are followed. The investigation of the unsteady large scale motion is carried out by means of snapshot analysis and by a statistical approach based on the spatial auto-correlation function. The Kelvin-Helmholtz (K-H) instability at the upper shear layer is observed to develop further with the onset of vortex pairing. The average distance between vortices is statistically estimated using the spatial auto-correlation. A marked transition with the wave-length increase is observed across the pairing regime. The K-H instability, initially observed only at the upper shear layer also begins to appear in the lower shear layer as soon as the wake is elevated sufficiently off the wall. The auto-correlation statistics confirm the coherence of counter-rotating vortices from the upper and lower sides, indicating the formation of vortex rings downstream of the pairing region.

---

[1] Ph.D. Candidate. Email: z.sun@tudelft.nl.

I. INTRODUCTION

The micro-vortex generator (MVG), also known as low-profile vortex generator [1] or sub-boundary layer vortex generator (SBVG) [2], is receiving increasing research interests in the area of aerospace engineering. Initially proposed for external aerodynamics applications, where it was placed on wing flap to enhance performance of high-lift configurations [3], the MVG is now also considered for internal flow systems, especially for supersonic air intakes, where shock wave boundary layer interaction (SWBLI) is encountered [4-6]. Flow separation may occur when the shock induced adverse pressure gradient is of sufficient strength to induce flow reversal. The flow separation associated to SWBLI is highly unsteady and introduces in turn undesired spatial and temporal fluctuations in the operation of the engine components placed downstream. In view of this, one of the primary objectives of MVG has been set to reduce flow separation and to stabilize the interaction region.

A number of baseline experimental studies have been carried out to investigate the effectiveness of MVGs towards SWBLI involving oblique or normal shock waves [7-9] and positive effects were confirmed. Additionally, fundamental studies of the flow induced by micro-ramps without the presence of SWBLI have been performed to aid the understanding of the physical mechanisms occurring inside the perturbed boundary layer. Much emphasis was placed on the description of the development of the MVG wake. Among them, Babinsky et al. [8] measured the cross-flow planes at three positions downstream of micro-ramps of various heights. The momentum deficit was visualized and its decay was also observed. The experimental study of Nolan & Babinsky [10] using laser Doppler anemometry (LDA) characterized the micro-ramp wake in further detail, revealing the quasi-circular shear layer wrapping the conical wake and the upwash and downwash motions induced by primary streamwise vortices. Downstream of 30 ramp heights the weaker imprints of these structures suggested a fast decay rate of the MVG wake. However the understanding of the dynamical organization of the turbulent flow field past the ramp in the far wake region is not yet achieved. One of the objectives of the present study is the investigation of the physical mechanisms occurring in the far wake that may be responsible for the regime of wake decay.

Numerical simulations by Lee et al. [11] using implicit large eddy simulation (ILES) described the decay of streamwise velocity component through the cross-sectional contours. A Reynolds-averaged Navier-Stokes (RANS) simulation with immersed-boundary treatment was performed by Ghosh et al. [12] (Ma=2.5, h/δ=0.46, 0.92) and the velocity profiles were compared with experiment data [8]. An acceptable agreement was only achieved for the larger micro-ramp (h/δ=0.92). As a result, further experimental study of the streamwise decay is needed not only for the reason of revealing the decay behavior but also to verify the ability of numerical simulations.

The time-averaged vortex structure behind a micro-ramp has already been described in terms of the mean flow topology. Babinsky et al. [8] identified a primary vortex pair dominating the mean flow and multiple secondary vortices of weaker strength. From the unsteady behavior of the wake, the clearest feature emerging from both experiments and simulations is the vortex shedding from the quasi-circular free shear layer emanating from the ramp trailing edge. Blinde et al. [13] inferred this from the wall-normal counter-rotating vortex pairs from the stereoscopic particle image velocimetry (Stereo-PIV) analysis in planes parallel to the wall. The numerical study of Li & Liu [14] showed that those vortices were rolled up from the growth of Kelvin-

Helmholtz (K-H) shear layer instability and finally developed into ring-shaped vortices. Further experimental evidence was provided by Lu et al. [15] who used the laser sheet visualization technique. Sun et al. [16] measured the three-dimensional structure of K-H vortices using tomographic PIV (Tomo-PIV). The experiments returned more an arch-like vortex rather than full ring or hairpin, which stands in some contrast to the work of Li & Liu [14] and Blinde et al. [13], respectively. More in particular, the discrepancy with the vortex ring model has not been reconciled so far and motivates the present study. The main hypothesis followed here is that the arch vortices may be able to reconnect on the bottom edge of the wake, achieving the annular shape.

Many studies report the rapid loss of coherence of bluff body wakes [17,18]. In line with this, the present investigation focuses on the regime that follows the part where coherent K-H vortices dominate the large-scale fluctuations in the free shear layer. At vortex breakdown and beyond, qualitative flow visualization techniques become increasingly difficult to interpret, due to the long time history of the smoke interface mixing. One of the main questions is whether the breakdown of arch- or ring-like vortices lead to a transition towards an isotropic regime and the disruption of the primary vortex pair, or that the latter is able to survive the break-up of arch/annular vortices. This would have important consequences for the long-range mixing capability of the micro ramp. Previous studies have not tackled the further evolution of the flow spatial organization and it is not clear in which conditions other structures can be generated from the train of K-H vortices by the pairing mechanism or by realignment of vortex filaments. In particular the vortex-pairing regime has not been identified or given attention by past literature.

With the purposes stated above, the current experiments are aimed at the characterization of the far wake (beyond 20 ramp heights) and a large measurement domain extending from approximately $12h$ to $32h$ is achieved making use of the planar PIV technique with large format CCD camera. In the attempt to draw some conclusions on the scaling laws for the wake decay, two values are investigated for the ratio between the micro-ramp height and the boundary layer thickness (h/δ). This is achieved by selecting ramps of 3 mm and 4 mm height respectively.

The following section describes the details of the experiments and measurement uncertainty. In the discussion of results, the decay of the micro ramp wake is elaborated through the time-averaged data and turbulent statistics. The analysis of the instantaneous realizations focuses on the observation of signatures of vortex pairing and vortex ring. Proofs are provided through spatial auto-correlation. At the end of the discussion, a conceptual model describing the vortical activity is delivered.

II. EXPERIMENTAL SETUP

A. Flow facility

The experiments were carried out in the wind tunnel ST-15 in the High-Speed Laboratory of the Delft University of Technology. The wind tunnel was operated at Mach 2.0 and the flow in the test section took about 2 seconds to stabilize. The duration for each measurement was approximately 70 seconds allowing 100 image-pairs to be recorded. The wind tunnel is fed by a compressed air reservoir of 400 m^3. During the blow-down operation the recorded temperature drop within each experiment was about 2°C, with negligible variation of the free-stream velocity. A separate planar PIV measurement dedicated to characterize the undisturbed turbulent boundary layer was carried out and reported previously [16]. After developing for approximately 1 m on the wind tunnel bottom wall, the boundary layer obtains a thickness of 5.2 mm in the test section. The displacement thickness δ^* and the momentum thickness θ were later determined to be 0.59 mm and 0.48 mm, respectively, resulting in an incompressible shape factor of H=1.2. The velocity profile of the undisturbed boundary layer is shown in figure 1. The free stream flow conditions and the properties of the boundary layer are summarized in table I.

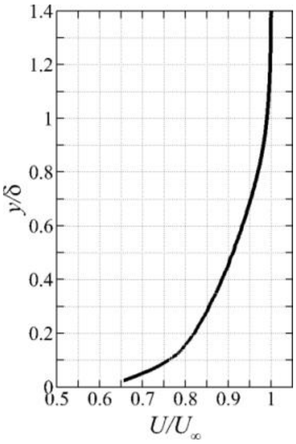

FIG. 1. Wall-normal profile of the streamwise velocity component in the undisturbed boundary.

TABLE I. Free stream flow conditions and undisturbed boundary layer properties.

Parameter	Quantity
Ma_∞	2.0 ± 0.02
U_∞	519 ± 4.2 m/s
δ	5.2 mm
δ^*	0.59 mm
θ	0.48 mm
H	1.2
Re_θ	13,600
Re_δ	1.47×10^5

B. Micro-ramps

The micro ramp geometry follows the configuration suggested by the work of Anderson et al. [19]. Two ramps are considered with heights of h=3 and 4 mm, corresponding to 57% and 77% of the undisturbed turbulent boundary layer thickness respectively. These two devices will be referred to as MR3 (h_3=3 mm) and MR4 (h_4=4 mm) in the remainder. The micro ramp chord length is c=7.5h and the half sweep angle is α=24°, the detailed geometrical dimension of the micro ramp is sketched in figure 2.

A single micro ramp was installed along the centerline of the wind tunnel test section bottom wall. The measurements were taken at the symmetry plane of each micro ramp. The origin of the coordinate system is placed at the junction of the micro-ramp trailing edge and the floor with x-axis pointing downstream and y-axis pointing away from the wall. The arrangement of the fields of view (FOVs) and their coordinates are shown together in figure 3.

FIG. 2. Side and top views of the micro-ramp geometry (MR3 and MR4).

FIG. 3. Arrangement of the FOVs for each micro ramp and the *x*-coordinates of the beginning and end of each FOV.

C. PIV instrumentation

Di-ethyl-hexyl-sebacate (DEHS) droplets with nominal diameter of approximately 1 µm were used as the seeding tracers. For these conditions (Mach 2.0 flow), a relaxation time of about 2 µs for the DEHS particles was determined by Ragni et al. [20]. The particles were injected into the settling chamber through a seeding probe with multiple orifices. The injection position was carefully chosen on the lower surface inside the settling chamber, thus a locally seeded stream tube was obtained, especially in the turbulent boundary layer.

The laser illumination in the FOVs was provided by a Spectra-Physics Quanta Ray double-pulsed Nd-Yag laser with 400 mJ pulse energy and 6 ns pulse duration at a wave-length of 532nm. A rigid periscope probe containing a combination of optics was used to introduce the laser beam into the test section, and it was vertically installed from the bottom wall downstream of the test section. Only the head part of the probe was exposed to the wind tunnel free stream with minimum blockage effects. As a result, the wind tunnel operated far from chocking conditions. By tuning the focus of the embedded optics inside the probe, the laser beam was formed into a thin sheet with approximately 2 mm thickness for the FOVs.

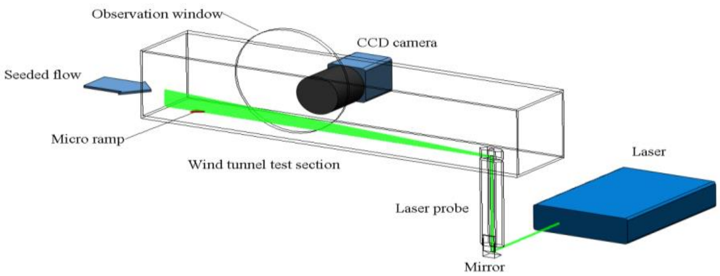

FIG. 4. The experimental setup: MVG, illumination layout and imaging configuration.

LaVision *Davis 8.0* software was used in the whole process of system synchronization, image acquisition and pre-processing, vector calculation and statistical post-processing. The images were pre-processed by the spatial sliding minimum subtraction and minimum-maximum intensity normalization. The particle image motion is made by iterative multi-grid image deformation. The resulting measurement grid is composed of 305×85 (MR3) and 305×72 (MR4) vectors with spacing of 0.23 mm (MR3) and 0.37 mm (MR4). The data post-processing eliminates spurious vectors with the universal median test [22] and replaces them by interpolation over the neighbor cells. The amount of spurious vectors did not exceed 5%.

D. Experimental uncertainty

In view of the utilization of the present data for comparison with numerical simulations or other experiments, an upper boundary is given here for the measurement uncertainty. It is considered that the uncertainty originating from PIV measurement dominates the overall experimental errors. The uncertainty due to the flow facility, such as temperature effects is verified to be negligible. The effects of the finite data ensemble size, the image analysis (cross-correlation) algorithm and finite particle tracers' response time [20] are considered here.

Each dataset is composed of 400 uncorrelated realizations. The uncertainty of averaged velocity components is estimated to be 0.8%U_∞ in the wake region where the largest velocity fluctuations occur. Accordingly, the uncertainty of $<u'>$ and $\overline{u'v'}$ were estimated to be 5%$<u'>_{max}$ and 12% $\overline{u'v'}_{max}$, respectively. The cross-correlation for planar PIV is assumed to have an uncertainty of 0.1 pixel [23], which corresponds to 0.5%U_∞. As a result, the uncertainty of the mean velocity is not affected by the measurement noise.

The measured vector field is given over a regular grid and each vector results from the cross-correlation over the kernel used for spatial cross-correlation. The current window size is about 20% of the wave-length of K-H wave and considering the given spatial response in [24], the expected amplitude modulation will not exceed 2%U_∞.

The response time of the DEHS tracer particle should also be considered. According to the experiment of Ragni *et al.* [20], the response time was estimated to be 1.92μs for DEHS particle. By multiplying the response time and the relevant particle acceleration, which is estimated to be 5×10^6 m/s^2 according to the centrifugal acceleration in the vortical motion, the uncertainty results to be approximately 2%U_∞.

III. RESULTS AND DISCUSSION

A. Decay of time-averaged velocity

The time-averaged velocity field is obtained by ensemble averaging the instantaneous measurements. Given the measurement repetition rate of 1.5Hz, the realizations are considered as uncorrelated. The streamwise and wall-normal coordinates are expressed in non-dimensional units using the ramp height as scaling length, following the study of Babinsky et al. [8], where the deficit loci from various micro ramps collapsed to a single curve. The decay of the streamwise and wall-normal velocity components are addressed first. Furthermore, the self-similar behavior of the wake is explored.

1. Streamwise velocity component

Similar flow fields are produced by both micro ramps, see the contours of streamwise velocity in streamwise range from x/h=12 to 32 in figure 5. The wake features a pronounced momentum deficit with a velocity minimum that moves away from the wall nonlinearly when developing downstream. The rate at which the maximum deficit is lifted off the wall decreases when moving downstream, as expected by the lower intensity of the upwash motion induced by the primary pair of streamwise vortices. A nearly horizontal wake is thus observed at the end of the measurement domain, similar as observed at approximately *x/h*=30 in the PIV study of Herges et al. [25] (Ma=1.4, *h/δ*=0.36). Different velocity magnitudes can be observed in the lower neck region, which is the region between the deficit and wall. Since the larger micro ramp (MR4) emerges more above the momentum thickness and the recirculation of high momentum fluid penetrates deeper at the bottom of the wake, higher magnitude is resulted there.

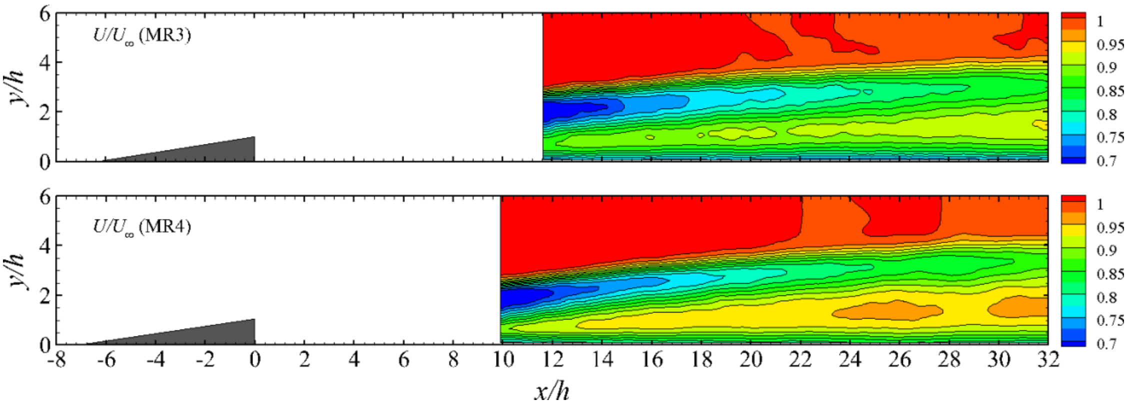

FIG. 5. Contours of streamwise velocity of MR3 (top) and MR4 (bottom).

A detailed analysis of the streamwise velocity evolution is achieved by extracting wall-normal profiles at three positions, i.e. *x/h*=12, 22 and 32, see figure 6. The maximum deficit at *x/h*=12 corresponds to a velocity of approximately 70% of the free-stream value and is located at two ramp heights (*y/h*=2). The wake recovery is dominated by the strong turbulent mixing occurring at the shear layer and the point of minimum velocity moves upward as a result of the coherent upwash motion. Simultaneously, the velocity defect is filled and flattened as a result of turbulent diffusion. Some discrepancy between the profiles of MR3 and MR4 can be observed, although the chosen scaling offers a better collapse when compared to scaling based on a boundary layer length scale. The aforementioned larger magnitude in the neck region of MR4 is represented by the mismatch of the boundary layer profiles, indicating that this part does not follow a scaling with the ramp dimensions.

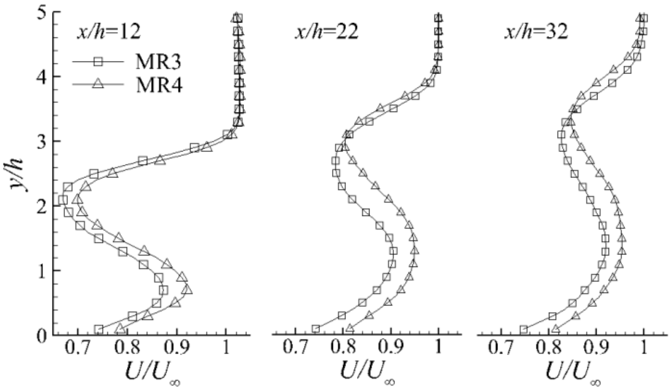

FIG. 6. Profiles of streamwise velocity at three positions of *x/h*=12, 22 and 32.

The streamwise velocity profile in the center plane has also been inspected in the previous LDA study of

Babinsky et al. [8] and RANS study of Ghosh et al. [12]. Both studies were carried out at Ma=2.5, but had slightly different height ratios, h/δ=1.0 for the LDA study and 0.92 for the RANS study. Streamwise velocity profiles at x/h=13.3 and 23.3 are compared with current measurements (see figure 7). The deficit region appeared at a lower position for a free stream condition at Ma=2.5. The profiles extracted from LDA measurements follow that of MR4 in the neck region, suggesting a similar rate of boundary layer recovery. A slower boundary layer recovery was predicted instead by RANS, which is especially evident at x/h=13.3. The position of the wake upper edge is clearly higher for the present experiments, which is partially ascribed to the smaller value of the height ratio (h/δ). However, also Mach number effect may need to be considered in this case as the reference data is based on free stream Ma=2.5 corresponding to a larger convective Mach number for the shear layer, as opposed to the present case.

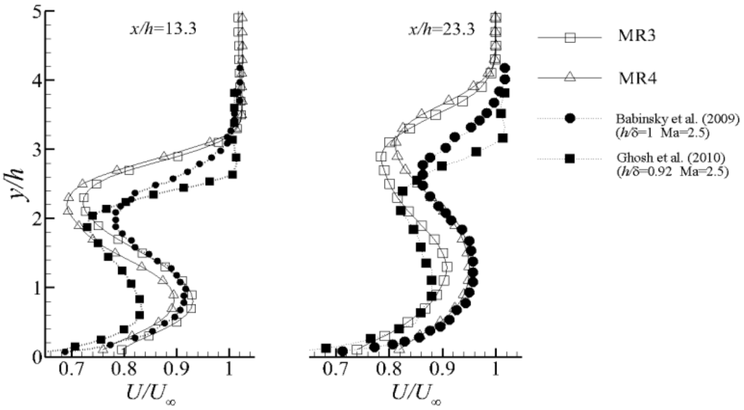

FIG. 7. Comparison of profiles of streamwise velocity at x/h=13.3 and 23.3. Profiles from Babinsky et al. [8] and Ghosh et al. [12] are reproduced from their original units.

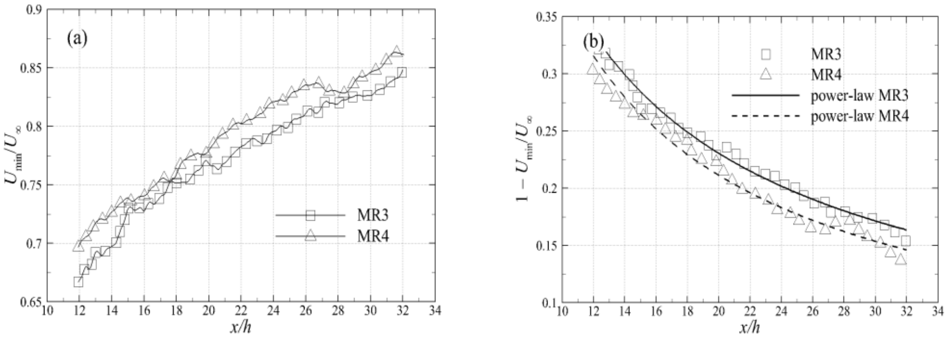

FIG. 8 Streamwise evolution of velocity deficit $U_{\min}/U_{\infty}$: (a) deficit velocity recovery; (b) decay of velocity difference between wake core and free stream $(U_{\infty}–U_{\min})/U_{\infty}$ and power-law fit.

A synthesis of the wake recovery is addressed by following the streamwise development of the maximum velocity deficit, see figure 8(a). Both ramps exhibit a similar recovery rate when expressed in non-dimensional coordinates, using the ramp height as scaling length. The minimum velocity $U_{\min}$ for MR4 increases from $0.7U_{\infty}$ at x/h=12 to $0.86U_{\infty}$ at x/h=32, while for MR3 it increases over this domain from $0.67U_{\infty}$ to $0.84U_{\infty}$.

According to the theoretical analysis given for fully turbulent plane and symmetric wakes[26], the velocity difference $(U_{\infty}–U_{\min})$ between the wake core and the outer stream follows a power-law decay with respect to the streamwise distance, namely $(U_{\infty}–U_{\min})\sim x^{-2/3}$. By performing the power-law fit to such velocity difference in the present wakes of MR3 and MR4 respectively (see figure 8(b)), their relations result as:

$$\begin{cases} \dfrac{U_{min}}{U_\infty} = 1 - 2.1\left(\dfrac{x}{h}\right)^{-0.73} & (MR3)(1a) \\ \dfrac{U_{min}}{U_\infty} = 1 - 2.2\left(\dfrac{x}{h}\right)^{-0.78} & (MR4)(1b) \end{cases}$$

As shown above, the exponents returned are 0.73 and 0.78 for MR3 and MR4, respectively. They are comparable but in excess to the value predicted from theory. The difference is ascribed to the presence of boundary layer turbulence that provides additional mixing. Therefore a more rapid recovery of the momentum deficit takes place. The slight difference of the exponents, instead, suggests that not all relevant scaling parameters are accounted for in the above experiments, e.g. the ratio of boundary layer momentum thickness and the ramp height (θ/h).

2. Wall-normal velocity component

The time-averaged wall normal velocity is studied in a similar scheme as streamwise velocity. In the center plane, an upwash region is coalesced from streamwise vortex pair, see the contours of wall-normal velocity in figure 9. Unlike the velocity deficit, the elevation of upwash is less steep. A much stronger upwash is produced by MR4 and it is associated to the stronger trailing vortex. The relation between the micro ramp height and vorticity intensity was reported in the ILES study of Lee et al. [27], where the maximum vorticity ($\omega_{x,max}$) and circulation dropped significantly when decreasing the height of micro-ramp into half.

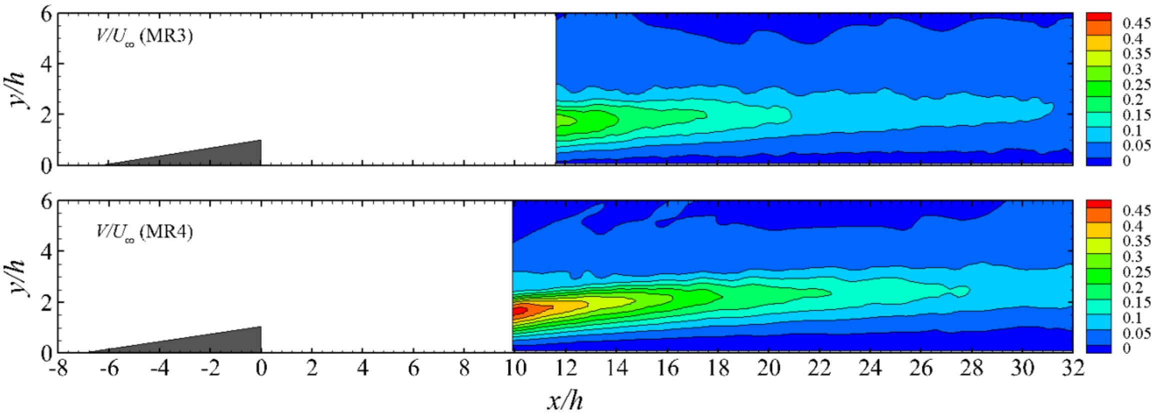

FIG. 9. The contours of wall-normal velocity of MR3 (top) and MR4 (bottom).

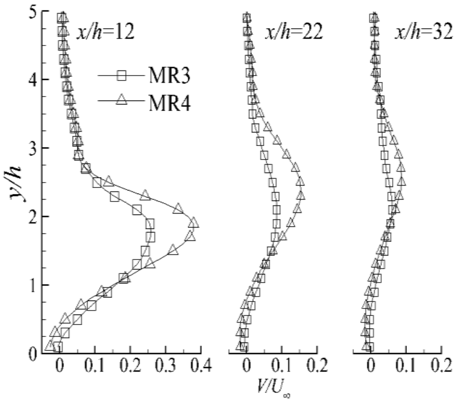

FIG. 10. Profiles of wall-normal velocity of MR3 and MR4.

The difference of the upwash strength is further addressed through the *V*-profiles, see figure 10. The significant mismatch of the *V*-profiles suggests the dependence of upwash intensity on the micro ramp size. At x/h=12, the V_{max} of MR3 is $0.25U_\infty$, which is 65% of that of MR4. Upwash recovery is obvious through the flattening of profiles, but it is more straightforward in the streamwise evolution of V_{max} in figure 11. The intensity discrepancy becomes smaller instead of being maintained. The narrowing discrepancy could be reasoned as the close strength of streamwise vortices of MR3 and MR4 regardless of their distinct magnitudes at upstream. As reported by Lee et al. [27], the vorticity generated by various MVGs was predicted to obtain similar strength at far downstream after x/h=30.

The upwash intensity is also considered to follow the power-law decay, thus power-law fit is performed again. The resulted relations are

$$\begin{cases} \dfrac{V_{max}}{U_\infty} = 20\left(\dfrac{x}{h}\right)^{-1.7} & (MR3)(2a) \\ \dfrac{V_{max}}{U_\infty} = 25\left(\dfrac{x}{h}\right)^{-1.6} & (MR4)(2b) \end{cases}$$

The fitted exponents for the peak upwash decay are much larger in absolute value, indicating a decay rate 2.5 times of that of deficit velocity. Unfortunately, in this case, no theoretical analysis is available for the streamwise evolution of this flow property.

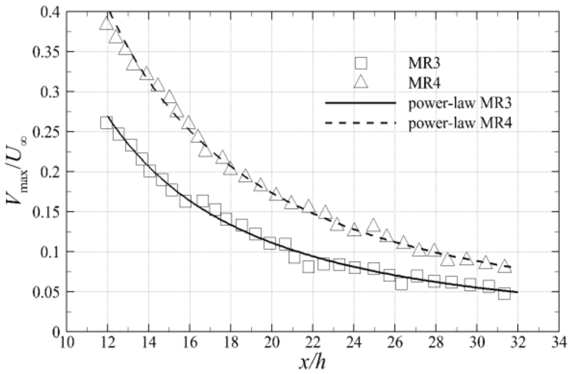

FIG. 11. Streamwise decay of maximum upwash velocity and power-law fit

In order to detect the relevance of the two significant flow structures, namely the deficit and upwash, the loci of U_{min} and V_{max} are compared, see figure 12. The U_{min} is observed to be produced higher instead of overlapping with V_{max}. The vertical offset suggests that the deficit center is not produced as soon as the peak upwash is reached, but is delayed.

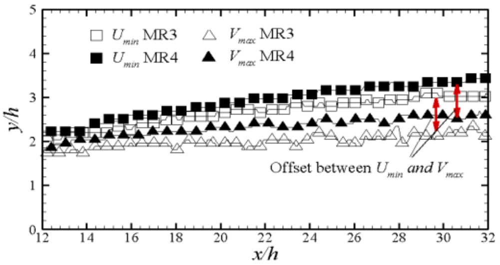

FIG 12. The loci of deficit center (U_{min}) and peak upwash (V_{max}) for MR3 and MR4.

3. Self-similarity of time-averaged velocity profiles

In order to study the possible self-similarity property of the time-averaged velocity profiles, a normalized form of the streamwise velocity component related to the wake velocity deficit can be defined as

$$\overline{U}(y) = \frac{U(y) - U_{BL}(y)}{\Delta U_{deficit}} \quad (3)$$

where $U(y)$ is the velocity in the controlled boundary layer, $U_{BL}(y)$ is velocity in the undisturbed boundary layer and $\Delta U_{deficit}$ ($\Delta U_{deficit}>0$) is the velocity difference between the maximum deficit and the corresponding position in the undisturbed boundary layer, see figure 13(a). By applying this type of normalization, the wake velocity magnitudes are scaled to the same range with maximum deficit being $\overline{U}_{deficit}=-1.0$. The y-coordinate normalization is done by first shifting the origin towards the maximum deficit position and then being divided by the height of maximum deficit ($y_{deficit}$):

$$\overline{y} = \frac{y - y_{deficit}}{y_{deficit}} \quad (4)$$

The resulted profiles subsequently have normalized $\acute{y}$-axis origin at the deficit center and $\acute{y}=-1$ at the wall position. The normalized profiles at x/h=12, 22, and 32 for both ramps are shown together in figure 14. A good degree of similarity is exhibited for the upper and lower shear layers in the deficit profiles.

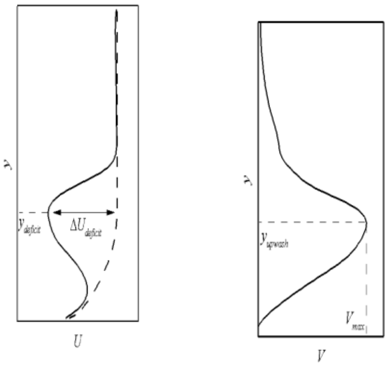

(a) (b)

FIG 13. Definitions of the quantities used in streamwise (a) and wall-normal (b) velocity normalizations.

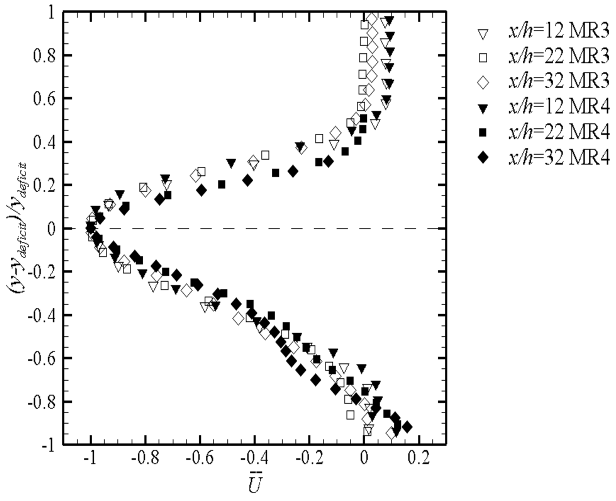

FIG. 14. Normalized profiles of deficit velocity at three positions.

The wall-normal velocity is normalized with the peak upwash velocity V_{max} following

$$\overline{V}(y) = \frac{V(y)}{V_{max}} (5)$$

so that the normalized peak upwash has a value of $\acute{V}_{upwash} = 1.0$. Similar as the normalization of the deficit profiles, the vertical coordinate of the upwash profile is also shifted towards the peak upwash and divided by coordinate of the peak upwash (y_{upwash})

$$\overline{y} = \frac{y - y_{upwash}}{y_{upwash}} (6)$$

Definitions of V_{max} and y_{upwash} are sketched in figure 13(b). In the resulted profiles, the peak upwash is located at $\acute{y}$=0 while the wall position at $\acute{y}$=-1. The normalized profiles at x/h=12, 22 and 32 are plotted in figure 15 where similar profiles are displayed. Based on the above observations, both the deficit and upwash profiles exhibit features of self-similarity using the described normalization velocity magnitude and length scale.

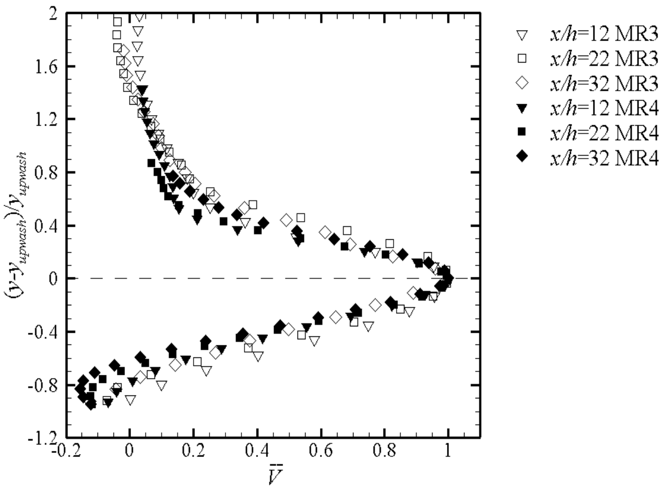

FIG. 15. Normalized profiles of upwash velocity at three positions.

B. Decay of turbulent properties

The decay of turbulent properties is investigated through assessing the development of the RMS of velocity components ($\langle u' \rangle$ and $\langle v' \rangle$) and the Reynolds shear stress ($\overline{u'v'}$). Next to documenting these properties, it will also be attempted to find possible self-similarity features of the decay revealed by appropriate scaling.

1. Velocity fluctuations

Increased level of velocity fluctuations occurs in the micro ramp wake, an overall observation can be achieved in the contours of $\langle u' \rangle$ and $\langle v' \rangle$ in figure 16 and 17, respectively. Note that in the figures the upper and lower edges of the wake defined by the inflection points in the velocity profiles are overlaid for reference by the gray lines. The velocity fluctuations follow the trend of the wake elevation, and the decay of fluctuation magnitude is evident from upstream to downstream. For example, $\langle u' \rangle_{max,MR4}$ is $0.06U_\infty$ at $x/h=32$ which is about 60% of the magnitude at $x/h=12$. The increased fluctuation within the wake was also measured by Herges et al. [25] using PIV and it was explained as a consequence of the streamwise vortices. However, current results reveal that peaks of $\langle u' \rangle$ and $\langle v' \rangle$ concentrate closer to the upper edge, where the K-H phenomenon dominates, and the enhanced fluctuation is more likely to be associated with this flow instability mechanism, which is able to undulate the flow through the embedded K-H vortices.

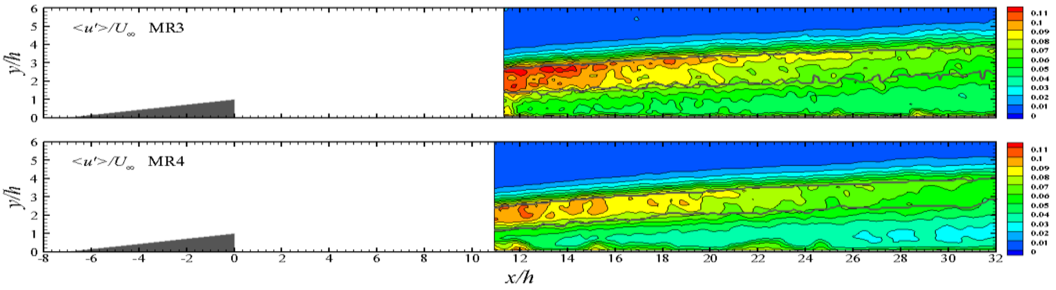

FIG. 16. The contours of $\langle u' \rangle$ for both micro ramps in nondimensional units.

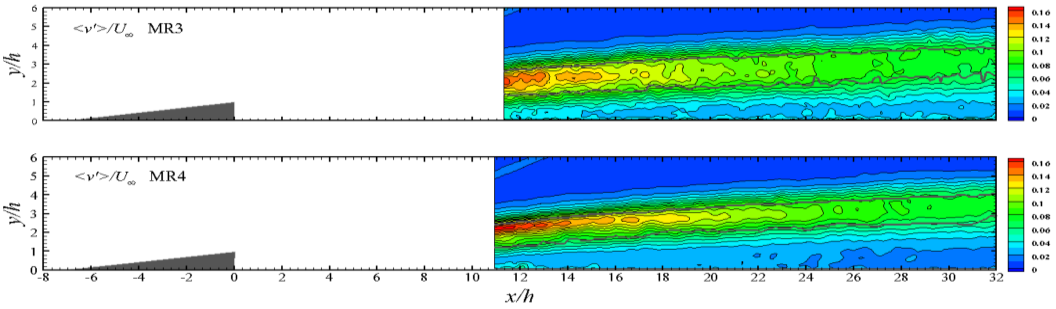

FIG. 17. The contours of $\langle v' \rangle$ for both micro ramps in nondimensional units.

More insights can be achieved from a further analysis of the profiles of $\langle u' \rangle$ and $\langle v' \rangle$. Considering the profiles of $\langle u' \rangle$ and $\langle v' \rangle$ at x/h=12, 22.8 and 32 in figure 18 and 19, the wake region corresponds to the portion within the profiles with elevated fluctuation levels. A comparison to the results of Herges et al. [25] (Ma=1.4, h/δ=0.36) at x/h=22.8 is made. In the profile of $\langle u' \rangle$, a similar upper-region peak was measured with a slightly stronger magnitude, whereas the lower part exhibited similar strength as the near wall region and no particular peak value was resolved. In the profile of $\langle v' \rangle$, an increased magnitude can be seen across the entire wake region, but with a lower intensity, about 60% of current measurement. Further comparison between $\langle u' \rangle$ and $\langle v' \rangle$ peak values reveals also a decrease in the anisotropy nature of the turbulence properties. At x/h=12, $\langle v' \rangle_{\max}$ is approximately 1.6 times of $\langle u' \rangle_{\max}$, suggesting strong anisotropy upstream. In contrast, comparable peak magnitudes, approximately $0.06U_\infty$, are achieved at x/h=32, which means the wake tends to behave more as isotropic turbulence in the later flow due to the wake decay.

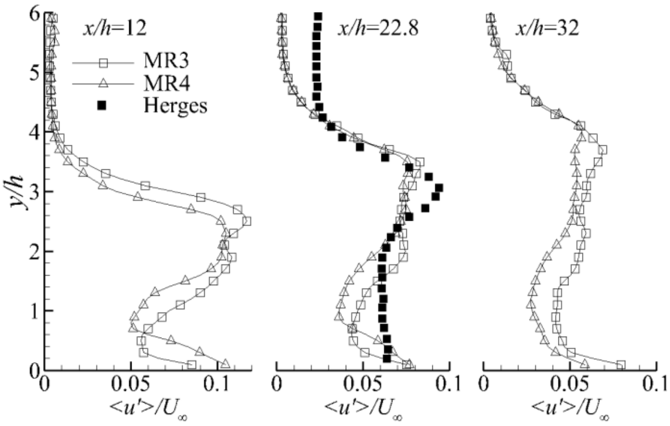

FIG. 18. Profiles of $\langle u' \rangle$ from MR3 and MR4 at x/h=12, 22.8 and 32. Results of Herges et al. [25] at x/h=22.8 are also included after adjustment into non-dimensional units.

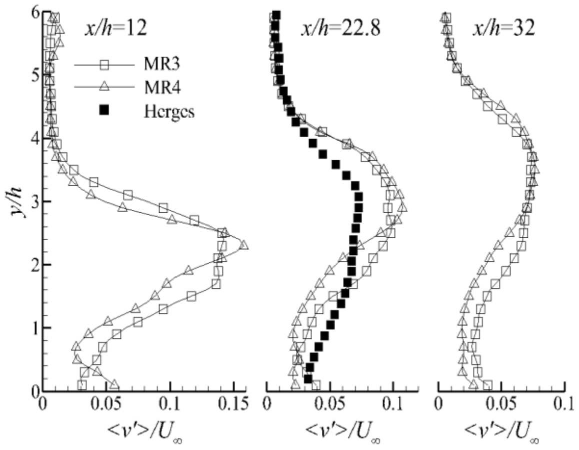

FIG. 19. Profiles of $\langle v' \rangle$ from MR3 and MR4 at x/h=12, 22.8 and 32. Results of Herges et al. [25] at x/h=22.8 are also included after adjustment into non-dimensional units.

2. Reynolds shear stress

The Reynolds shear stress $\overline{u'v'}$ is a measure of the turbulent mixing activity in the flow and generated by mean flow shearing effects. Concentration of negative peaks are thus produced along the upper edge, see figure 20. Symmetric peaks of positive value can also be observed. They are above the lower edge in the first half of current FOV, and start to fall over the lower edge in the next half. Comparison of the loci of quantities including $(\overline{u'v'})_{\max}$, $(\overline{u'v'}_{\min}$ and $V_{\max}$ gives the relations among them. The three loci of MR4 are shown in figure 21, making evident that $(\overline{u'v'}_{\max}$ follows $V_{\max}$. As a result, the positive peaks of $\overline{u'v'}$ is more likely associated with the event of peak upwash instead of the lower wake shear layer. The $\overline{u'v'}$ profile from Herges *et al.* [25] at *x/h*=22.8 is also compared with current measurement, see figure 22. Negative Reynolds shear stress was measured to dominate the whole wake with a similar magnitude as current experiments, whereas no evidence of positive peak was measured, possibly due to the lower upwash magnitude (see figure 19).

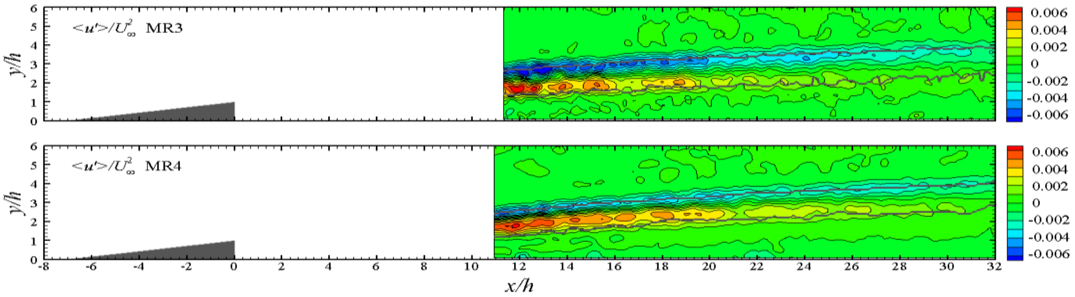

FIG. 20. Contours of Reynolds shear stress $\overline{u'v'}$ of both ramps in nondimensional units.

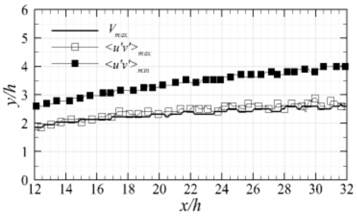

FIG. 21. Loci of $(\overline{u'v'}_{min}$, $(\overline{u'v'}_{max}$ and V_{max} from MR4.

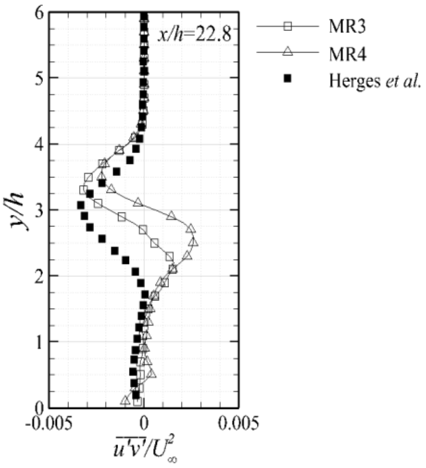

FIG. 22. Comparison of profiles of $\overline{u'v'}$at *x*/*h*=22.8, the profile from Herges *et al*. [25] is included after adjustment into non-dimensional units.

3. Self-similarity of turbulent quantities

In order to explore the possible scaling and self-similarity of the turbulent quantities, the velocity fluctuations are normalized with their peak values following

$$\overline{\langle u' \rangle} = \frac{\langle u' \rangle}{\langle u' \rangle_{max}} (7) \overline{\langle v' \rangle} = \frac{\langle v' \rangle}{\langle v' \rangle_{max}} (8)$$

Since there are symmetric peaks of Reynolds shear stress, it is normalized with the difference between the two peak values using

$$\widetilde{u'v'} = \frac{\left(\overline{u'v'}\right)}{\Delta\left(\overline{u'v'}\right)} (9a)$$

$$\Delta\left(\overline{u'v'}\right) = \left(\overline{u'v'}\right)_{max} - \left(\overline{u'v'}\right)_{min} (9b)$$

Considering the increased fluctuation mainly concentrates within the wake region, the normalized profiles are shifted towards the center of the wake, which is the average of the upper edge and lower edge positions. The height of the wake center is chosen as the spatial normalization scaling. The normalization of vertical distance can thus be expressed as

$$\overline{y} = \frac{y - y_{center}}{y_{center}} (10a)$$

$$y_{center} = \frac{1}{2}\left(y_{up} + y_{low}\right) (10b)$$

where y_{center} is the *y*-coordinate of wake center, y_{up} and y_{low} are the *y*-coordinates of upper and lower edges respectively (defined on the basis of the inflection point in the velocity profile).

The normalized profiles of $\overline{\langle u' \rangle}$,$\overline{\langle v' \rangle}$ and $\widetilde{u'v'}$are shown in figure 23(a)~(c), respectively. A good degree of similarity are exhibited by the profiles under current scaling parameters, although slight scattering effect can be observed within the wake region.

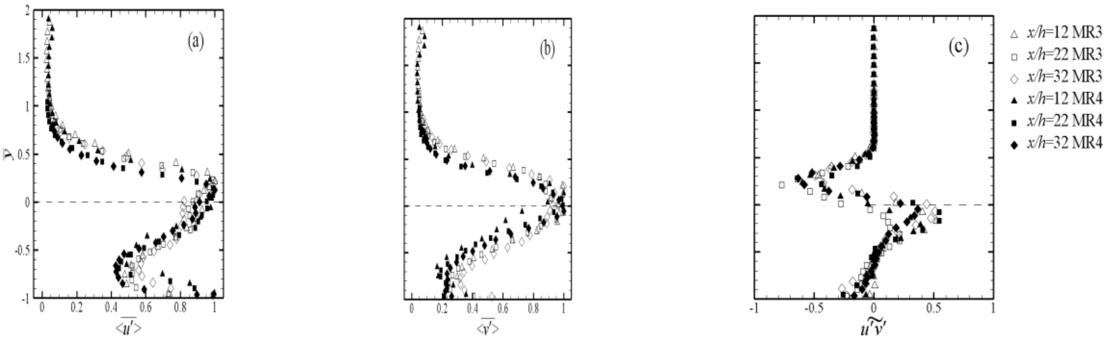

FIG 23. The normalized profiles of turbulent quantities at three positions: (a) the normalized streamwise velocity fluctuation $\overline{\langle u' \rangle}$, (b) the normalized wall-normal velocity fluctuation $\overline{\langle v' \rangle}$; (c) the normalized Reynolds shear stress $\widetilde{u'v'}$.

C. The instantaneous flow structure

The instantaneous flow behaves distinctively from the mean flow and prominently features the presence of the K-H instability, see one flow realization of MR4 in figure 24. The K-H instability is characterized by the wave-like structure at the top of the wake, and a train of vortex is shed following the development of the unstable wave. The swirling vectors of the K-H vortices in a convective reference frame are visualized in figure 25 by subtracting a constant value of $0.87U_\infty$ from the streamwise vector component. The vortex shedding is a common phenomenon existing in the wake of a bluff body, and a large body of studies have been devoted into this phenomenon [17,18]. However in the micro ramp flow, this phenomenon has received only moderate attention until the studies of Li & Liu [14], Lu *et al.*[15] and Sun *et al.* [16]. One immediate result from the vortical activity is the distortion of the velocity field, which consequently results in local high speed and low speed packets on either side of the K-H wave. The relatively long streamwise extent of the current study allows the study of the subsequent flow development, in particular the occurrence of the vortex paring which is a typical event occurring in the later stages of vortex shedding instabilities. Since at downstream the wake is lifted sufficiently away from the wall, which reduces the interface with turbulent flow in the direct vicinity of the wall, the exploration of the possible flow instability is more easily accomplished.

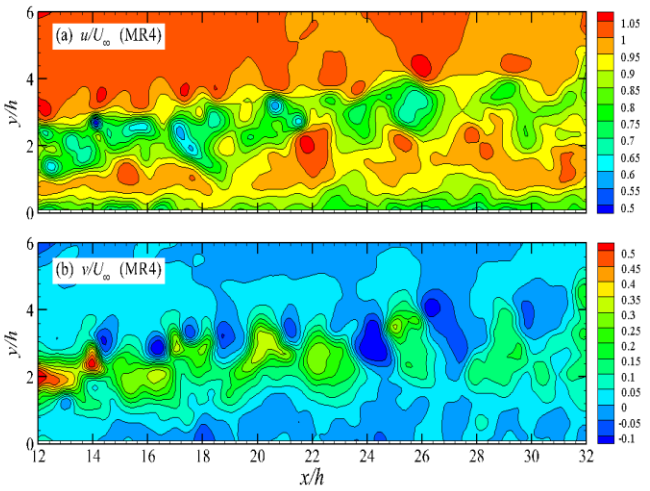

FIG 24. The instantaneous flow field: (a) contour of *u*; (b) contour of *v*.

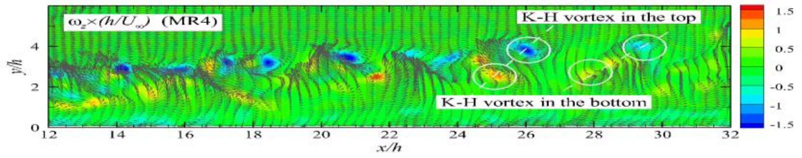

FIG. 25. The instantaneous vorticity field. Vortices are visualized in a convective frame by subtracting a value of $0.87U_\infty$ from the streamwise component.

1. Vortex pairing

Vortex pairing is featured with a pair of closing-up vortices in the process of vortex shedding and subsequently results in a larger wave-length downstream after the merge of the previous two. One pair of vortices which are about to merge can be seen at around *x/h*=23 in figure 25. This region is also enlarged in figure 26, and the two pairing vortices have a distance of about 1*h*.

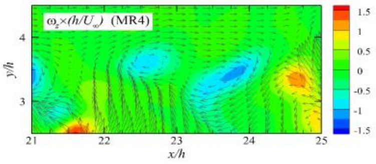

FIG. 26. The close-up view of vortex pairing in figure 25.

In order to identify the onset of vortex pairing and the evolution of the wave-length, auto-correlation of the instantaneous vorticity field is adopted. The procedure of auto-correlation is the same as that used in [16] according to the following expression:

$$c_n(\delta x, \delta y) = \sum_{i=0}^{M}\sum_{j=0}^{N}[\omega_n(i,j) \times \omega_n(i+\delta x, j+\delta y)] \ (11a)$$

$$C = \sum_{n=1}^{NF} c_n \ (11b)$$

where ω_n is the vorticity intensity in the n-th snapshot, c_n is the auto-correlation map of an individual snapshot and C is the summation of auto-correlations in the entire dataset containing NF snapshots. Note that the positive vorticity magnitudes are filtered out before the auto-correlation operation. For the current purpose, the auto-correlation window is shifted towards various streamwise positions. Different auto-correlation window sizes have been used to exclude the error associated with window size (*WS*). A three-dimensional representation of the auto-correlation result is shown in figure 27. Note that the central peak P_0 in figure 27 is very large and exceeds the current range. There are two prominent secondary positive peaks symmetric to the central one. The wave-length is thus determined by measuring the distance between the central peak and either of the two secondary peaks.

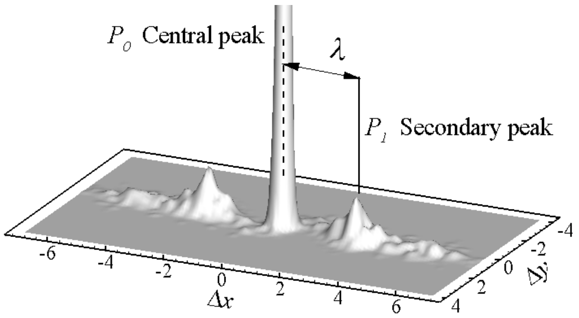

FIG. 27. Three-dimensional representation of the auto-correlation peaks in *x/h*=18.5~25.5 of MR4.

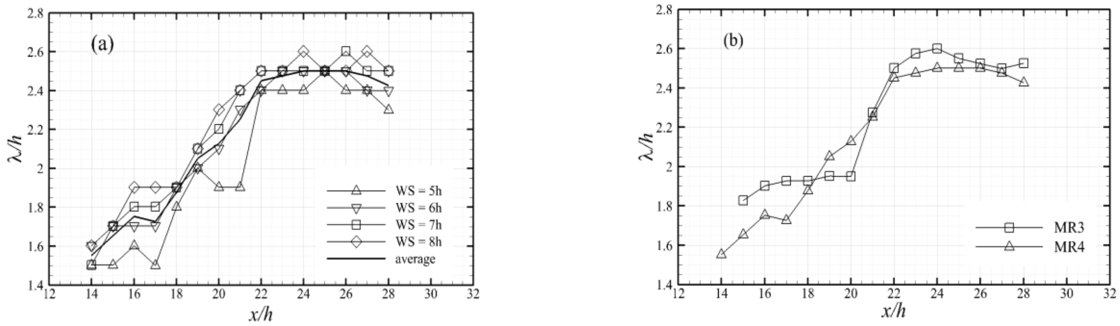

FIG. 28. The wave-length evolution (a) Wave-length evolution of MR4 retrieved using four window sizes; (b) The averaged wave-length evolutions of MR3 and MR4.

The wave-length evolutions of MR4 retrieved using four different *WS*s, namely *WS/h*=5,6,7,8 are presented in figure 28(a). Similar evolution trends are returned by most window sizes, although scatter exists. Further averaging of the wave-length evoloution retrived from the valid *WS*s provides a smoothed result, see figure 28(b). The wave-length is approximately 1.8*h* and 1.7*h* for MR3 and MR4 respectively at *x/h*=15. An evident jump occurs at around *x/h*=20 and the wave-length increases to about 2.5*h* till *x/h*=28.

The wave-length evolution is, on one hand, associated with vortex motion speed in the shear layer, which is determined by the mean shear velocity. In the current case, the mean shear velocity in the upper shear layer increases from $0.73U_\infty$ to $0.82U_\infty$ in the range of *x/h*=16~28 for MR3, whereas it increases from $0.74U_\infty$ to $0.83U_\infty$ in the same range for MR4. Hence a mean shear velocity increase ratio $\acute{U}_{x/h=28}/\acute{U}_{x/h=16} = 1.1$ is resulted for both MR3 and MR4. The distance between two vortices should grow naturally following the vortex speed increase. Ideally the downstream wave-length should be about 1.1 times of the upstream one provided that no vortex pairing takes place.

According to the current wave-length evolution as revealed in figure 28(b), the wave-length increases at a larger ratio of 1.32 and 1.46 for MR3 and MR4 respectively in the region of *x/h*=16~28. The larger actual increase ratio is cosidered to be also influenced by vortex pairing, which is supposed to increase wave-length by a factor of 2. In order to reveal the occurance of vortex pairing, probability densities of the wave-length calculated in streamwise windows (window size *WS*=7*h*) centered at *x/h*=16, 22 and 28 are shown in figure 29. It is apparent that the dominant wave-length shifts approximately from $2h$ to $2.5h$, which is because of the natural increase of mean shear velocity. The doubled wave-length ($\lambda_{double}/h \approx 3.5$) caused by vortex pairing amounts to about 7% in the upstream region of *x/h*=12.5~19.5, and it increases gradually to about 10% in the the region of *x/h*=18.5~25.5 and eventually stays at 17% and 12% in the last region for MR3 and MR4 respectively. Therefore, the vortex pairing takes place with greater probability in the far downstream.

Note that there are also very large and very low values of wavel-length occurring in the probability histograms, although they only constitute a small fraction. In order to explain the cause of the two extremes, a typical auto-correlation result is firstly shown in figure 30(a), where the decreasing peaks represent the regularly alinged K-H vortices along the upper shear layer. The very large value of wave-length is resulted from an auto-correlation as shown in figure 30(b). Although a peak close to the central one is resolved, it has a smaller intensity than the most outward one. As a result, the wave-length is determined to be the distance between the central peak and most outward peak, namely 4.2h in the current case. This case is considered as a consequence of the higher uncertainty of vorticity quantity. Similarly, the very small value of wave-length is associated with a stronger peak very close to the central one. Physically, this may happen when two strong K-H vortex are rather close, namely vortex paring is taking place. The occurances of the very large and very small values in turn give rise to the slight fluctuation of wave-length as shown in the downstream region (*x/h*=22~28) in figure 28(b).

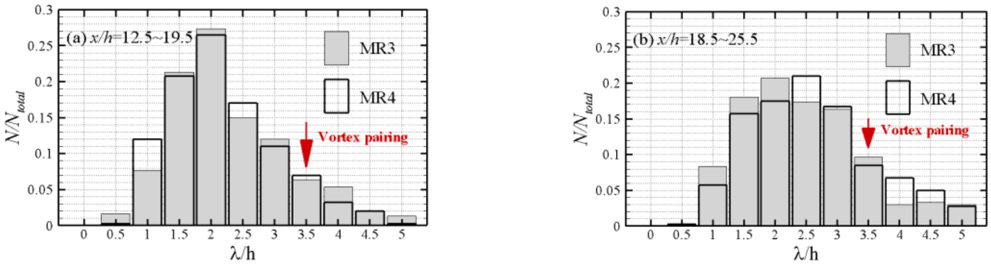

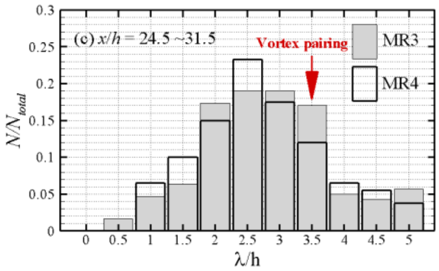

FIG. 29 Probability densities of wave-length retrieved by vorticity field auto-correlation in three streamwise windows (window size *WS/h*=7) centered at (a) *x/h*=16; (b) *x/h*=22; (c) *x/h*=28.

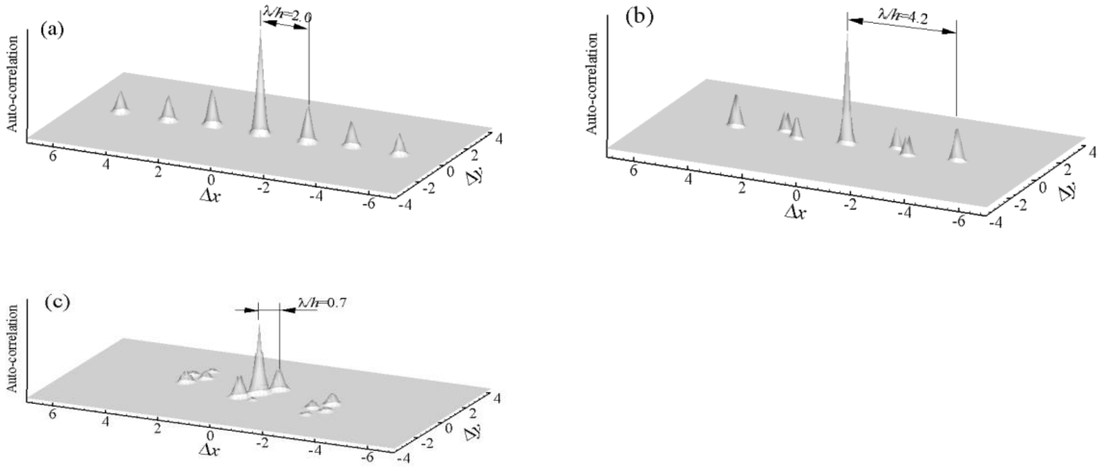

FIG. 30 Auto-correlation results of instantaneous vorticity snapshots: (a) typical wave-length; (b) very large value of wave-length; (c) very low value of wave-length.

2. Vortex generation in the lower part

Wavy pattern and associated high speed packets, resembling that on the upper part, can also be observed in the lower region of current FOV from approximately x/h=15 in figure 24, which is beyond the previous experiment [16]. These structures at the lower part also resemble the features of the K-H instability. They occur when the wake is lifted sufficiently away from the wall so that the unstable wave in the remaining parts of the wake interface is allowed to penetrate into the bottom region. The micro ramp wake is therefore fully wrapped by the corrugated surface in this downstream region.

In the vortical field, vortices with counter rotation relative to the ones in the upper shear are consequently produced in the lower region. According to the observation of the entire ensemble, the vortices in the lower layer appear in pair with the K-H vortices in the upper wake, which suggests that the arch-shape K-H vortex could be connected from the bottom and features a full ring. The vortical field in figure 25 is one example, where two apparent pairs of vortices can be seen close to the end of the domain.

In order to give further statistical support to this hypothesis of vortical activity and vortex ring formation, the auto-correlation of the vorticity field is computed within three regions, namely (12~19)h, (18.5~25.5)h and (25~32)h, corresponding to the different wake development phases, referred to as Region I~III respectively. The size of auto-correlation window is chosen to be $7h\times4.5h$, which is wide enough according to the *WS* effect test in the previous section. Since positive correlation peak suggests the spatial relation of the K-H vortices in the upper shear layer, the negative peak is thus a proof of the spatial correlation between the vortices in the upper and lower layers.

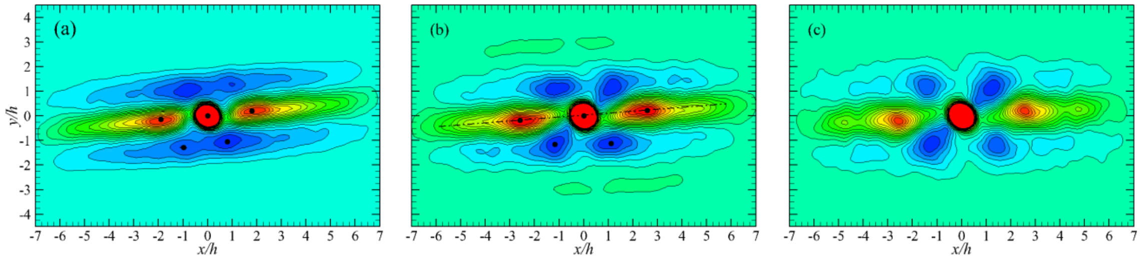

FIG. 31. Contour maps of auto-correlation: (a) Region I x/h=12~19; (b) Region II x/h=18.5~25.5; (c) Region III x/h=25~32.

The auto-correlation maps of Region I~III are explored in detail, see figure 31 for the results of MR4. The triple-positive-peak structure appears in all the three regions, and the wave-length is estimated to be λ_1 = 2.0h, 2.6h and 2.6h respectively. The apparent increase of wave-length is driven by mean shear velocity increase and vortex pairing, as discussed before. Isolated sharp negative peaks can be seen in Region II and III. The vortex with positive vorticity in the lower layer are thus produced together with the one in the upper layer forming a forward inclination of about 45° in both regions. By measuring the distance between the two negative peaks, the wave-length in the lower layer is λ_2=2.8h, slightly larger than λ_1. A different pattern of negative correlation is observed in Region I, where the negative peaks are not as sharp as in Region II and III. Thus the stripe region highlighted with negative correlation suggests that the occurrence of vortex shedding is not correlated with upper layer vortex. Since at downstream the two counter vortices obtain close correlation, they can be considered as imprints of a ring K-H vortex in agreement with the ring vortex model proposed by Li & Liu [14].

IV. A Conceptual Model

To consolidate the analysis on the vortical activity in the developing micro ramp wake, a conceptual model describing the evolution of vortical organization is presented in figure 32. In this model, the previous K-H vortex descriptions of Li & Liu [14] and Sun et al. [16] are incorporated and considered as partial stages or elements of the K-H vortex evolution. In the immediate downstream of the micro ramp, the streamwise vortices may occur as focused filaments. The curved free shear layer around the wake, however, quickly becomes unstable and the associated arch-shape K-H vortex are generated. According to the observation with Sun et al.[16], the streamwise filaments may merge with the leg portions of the K-H vortex. Further downstream, following the mean shear velocity increase and vortex pairing, the wave-length of instability phenomenon is increased. Due to the downward motion induced by the streamwise vortices, the leg portions of these arch-shape K-H vortices extend to the bottom side of the turbulent wake, which eventually leads to the vortex ring formation in the far wake. The process of vortex ring formation is illustrated in the bottom right of figure 32. Speculation can be made to the wake downstream of current measurement extent. The ring vortex will be subject to turbulent distortion and eventually breaks down. Accompanying the evolution of K-H vortex, the streamwise vortices decay at a fast rate and are rather weak.

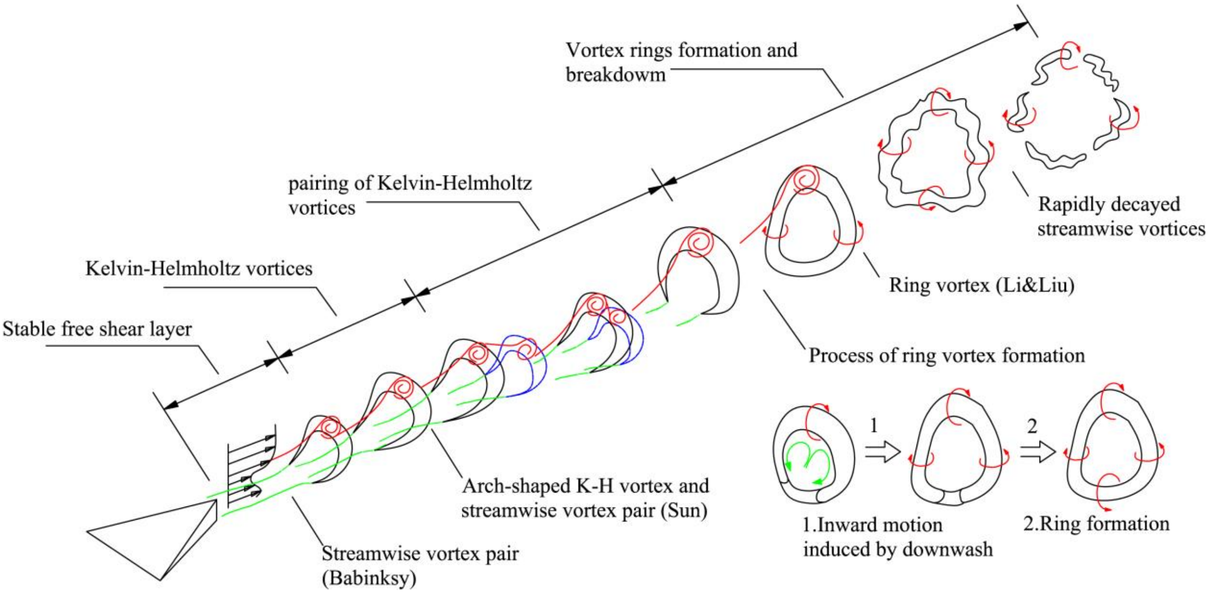

FIG. 32. The conceptual model of the vortical organization in the micro ramp wake.

V. Conclusions

Based on the reported results of the time-averaged velocity, the turbulent statistics and the statistical analysis of the instantaneous flow fields, the properties of the micro ramp wake decay at the center plane and the associated vortical activity can now be summarized.

Scaling the streamwise distance with the micro ramp height, similar magnitude of the streamwise velocity deficit is produced by the considered micro ramps, whereas a stronger upwash is generated by the larger micro ramp, which is ascribed to the stronger streamwise vortices resulting from that device. The streamwise velocity deficit and the upwash exhibit different rates of decay. Comparing the loci of maximum deficit and peak upwash, the former occurs at a higher location.

Anisotropy of velocity fluctuation is observed in the micro ramp wake at upstream with $\langle v' \rangle$ stronger than $\langle u' \rangle$, whereas both quantities obtain similar intensity at downstream due to the faster decay of $\langle v' \rangle$. The Reynolds shear stress $\overline{u'v'}$ in the center plane obtains near symmetric peaks. The negative peak is associated to the vortex production and follows closely the position of upper shear layer, while the positive peak is likely to be associate to upwash activity as loci of $(u'v')_{max}$ and $V_{\max}$ overlap. For each of the two time-averaged velocity components and the three turbulent quantities, the normalized profiles overlap with acceptable degree respectively, suggesting a possible self-similarity properbility.

In the instantaneous flow, the well-organized time-averaged flow is greatly affected by the K-H instability and the vortical flow obtains great complexity. Observation of the instantaneous realizations as well as the wave-length evolution retrieved from statistical spatial auto-correlation confirm the vortex pairing, which determines the transition of the micro ramp wake. Apart from the instability of the upper layer, the elevation of the wake allows the vortex generation mechanism to penetrate also into the lower region of the conical wake. The present data provides experimental support that this ultimately leads to a vortex ring formation from the connection of the arch-shape K-H vortex.

ACKNOWLEDGEMENT

This work is sponsored by China Scholarship Council (No. 2009629106)

REFERENCES

[1] Lin, J. C., Review of research on low-profile vortex generators to control boundary-layer separation, Progress in Aerospace Sciences, 38(4-5), 2002, 389-420.

[2] Ashill, P. R., Fulker, J. L. and Hackett, K. C., Research at Dera on sub boundary layer vortex generators(SBVGS), AIAA paper 2001-887.

[3] Lin, J. C., Robinson. S. K. and McGhee, R. J., Separation control on high-lift airfoils via micro-vortex generators, J. Aircraft, 31(6), 1994, 1317-1323.

[4] Rybalko, M., Loth, E., Chima, R.V., Hirt, S.M. and DeBonis, J.R., Micro-ramps for external compression low-boom inlets, AIAA paper 2009-4206.

[5] Hirt, S.M., Chima, R.V., Vyas, M.A., Wayman, T.R. and Conners, T.R., Experimental investigation of a large-scale low-boom inlet concept, AIAA paper 2011-3796.

[6] Galbraith, D.S., Galbraith, M.C., Turner M.G., Orkwis, P.D. and Apyan A., Preliminary numerical investigation of a Mach 3 inlet configuration with and without aspiration and micro-ramps. AIAA paper 2010-1095.

[7] Holden, H. and Babinsky H., Effects of microvortex generators on the separated normal shock/boundary layer interactions, J. Aircraft, 44(1), 2007, 170-174.

[8] Babinsky, H., Li, Y. and PittFord, C. W., Microramp control of supersonic oblique shcok-wave/boundary-layer interactions, AIAA J., 47(3), 2009, 668-675.

[9] Titchener, N. and Babinsky, H., Microvortex generators applied to flowfield containing a normal shock wave and diffuser, AIAA J., 49(5), 2011, 1046-1056.

[10] Nolan, W. R. and Babinsky, H., Characterization of mico-vortex generators in supersonic flows, AIAA paper 2011-71.

[11] Lee, S., Goettke, M.K., Loth, E., Tinapple, J. and Benek, J., Microramps upstream of an oblique-shock/boundary-layer

interaction, AIAA J., 48(1), 2010, 104-118.

[12] Ghosh, S., Choi, J-I and Edwards, J., Numerical simulations of effects of micro vortex generators using immersed-boundary methods, AIAA J., 48(1), 92-103.

[13] Blinde, P. L., Humble, R. A., van Oudheusden, B. W. and Scarano, F., Effects of micro-ramps on a shock wave/turbulent boundary layer interaction, Shock Waves, 19(6), 2009, 507-520.

[14] Li, Q. and Liu, C., LES for supersonic ramp control flow using MVG at M=2.5 and Re_θ=1440, AIAA paper 2010-592.

[15] Lu, F. K., Pierce, A. and Shih, Y., Experimental study of the near wake of micro vortex generators in supersonic flow, AIAA paper 2010-4623.

[16] Sun, Z., Schrijer, F. F. J., Scarano, F. and van Oudheusden, B. W., The three-dimensional flow organization past a micro-ramp in a supersonic boundary layer, Phys. Fluids, 24(5), 2012, 055105-22.

[17] Cimbala, J.M., Nagib, H.M. and Roshko, A., Large structure in the far wakes of two-dimensional bluff bodies, J. Fluid Mech., 190(2), 1988, 265-298.

[18] Prasad, A. and Williamson C.H.K., Three-dimensional effects in turbulent bluff-body wakes, J. Fluid Mech., 343(), 1997, 235-265.

[19] Anderson, B. H., Tinapple H. and Surber, L., Optimal control of shock wave turbulent boundary layer interactions using micro-array actuation, AIAA paper 2006-3197.

[20] Ragni, D., Schrijer, F.F.J., van Oudheusden, B. W. and Scarano, F., Particle tracer response across shocks measured by PIV, Exp. Fluids, 50(1), 2011, 53-64.

[21] Elsinga, G., van Oudheusden, B.W. and Scarano, F., Evaluation of aero-optical distortion effects in PIV, Exp. Fluids, 39(2), 2005, 246-256.

[22] Westerweel, J. and Scarano, F., Universal outlier detection for PIV data, Exp. Fluids, 39(6), 2005, 1096-1100.

[23] Westerweel, J., Digital particle image velocimetry, Doctoral thesis, Delft University of Technology, 1993.

[24] Schrijer, F.F.J. and Scarano F., Effect of predictor-corrector filtering on the stability and spatial resolution of iterative PIV interrogation, Exp. Fluids, 45(5), 2008, 927-941.

[25] Herges, T., Kroeker, E., Elliott, G. and Dutton, C., Microramp flow control of normal shock/boundary-layer interactions, AIAA J., 48(1), 2010, 2529-2542.

[26] Tennekes, H. & Lumley, J.L., A first course in turbulence, MIT Press, 1972.

[27] Lee, S., Loth, E., Georgiadis, N.J. and DeBonis, J.R., Effect of Mach number on flow past micro-ramps, AIAA J., 49(1), 2011, 97-110.